



Combustion mode and wave multiplicity in rotating detonative combustion with separate reactant injection

Majie Zhao^a, Matthew J. Cleary^b, Huangwei Zhang^{a,*}

^a Department of Mechanical Engineering, National University of Singapore, 9 Engineering Drive 1, Singapore 117576, Republic of Singapore

^b School of Aerospace, Mechanical and Mechatronic Engineering, The University of Sydney, NSW 2006, Australia



ARTICLE INFO

Article history:

Received 23 May 2020

Revised 1 November 2020

Accepted 2 November 2020

Keywords:

Non-premixed reactant

Rotating detonation combustion

Combustion mode

Reactant mixing

Multiple detonation waves

ABSTRACT

Numerical simulations with detailed chemistry are conducted for two-dimensional rotating detonative combustion with separate injection of fuel and oxidant. The influences of the fuel and oxidant compositions on combustion mode and detonation wave multiplicity are studied. It is found that in the parts of the flow beyond the fuel refill zone, there are two distinct, highly inhomogeneous zones with fuel-rich and fuel-lean compositions, respectively. Both detonative and deflagrative regimes are observed and proceed mostly under a premixed combustion mode with the deflagration confined mostly to the fuel-lean zone. The results from our simulations show that limited H_2 is detonated or deflagrated close to stoichiometric conditions and more than 70% of H_2 is detonated or deflagrated under fuel-lean conditions. Over 70% of the detonated H_2 is consumed in a premixed combustion mode. Our analysis also suggests that the detonation fraction increases with increased inlet pressure, decreased inlet temperature or increased injection orifice number. Additionally, the range of mixture fraction over which the composition is detonable is narrower than the range for deflagration. The number of detonation waves increases with increased oxygen mass fraction in the oxidant stream, with the additional waves being formed by mutual enhancement of an explosive hot spot and a travelling shock wave. Stabilization of the multiple waves follows a chaotic period involving both co-rotating and counter-rotating waves. Furthermore, the deficit of the detonation speed relative to the ideal Chapman–Jouguet value increases with the number of waves but also decreases monotonically with the level of reactant mixing. The reactant mixing effects along the detonation wave height are further discussed through quantifying the statistics of height-wise mixture fraction, heat release rate and OH mass fraction.

© 2020 The Combustion Institute. Published by Elsevier Inc. All rights reserved.

1. Introduction

The efficiency of detonation engine cycles can be up to 19% higher than that of engine cycles based on deflagrative combustion [1]. Compared to pulse detonation engines, the Rotating Detonation Engine (RDE) concept has numerous advantages, including its compact configuration, the continuous existence of Rotating Detonation Waves (RDW's) and avoidance of cyclic deflagration-to-detonation transitions, high frequency and high specific power [1,2]. The fundamental physics of Rotating Detonation Combustion (RDC) relevant to RDE configurations has been studied through theoretical analysis, experimental measurements and numerical simulations, and the latest research progress is summarized in several detailed reviews, for instance, by Anand and Gutmark [1], Wolanski [2],

Kailasanath [3], Lu and Braun [4], and Zhou et al. [5]. Although the first successful RDE operation [6] used premixed propellant injection, separate injection of fuel and oxidant is more desirable due to the inherent safety advantages [1].

RDC with separate reactant injection has been achieved with varying degrees of success for different combustor configurations, fuel types and operating conditions [7–16]. However, there are still significant challenges that must be tackled before such RDE's can be commercialized. Chief among these challenges is the need to rapidly mix the propellant in the fuel refill zone of the combustor to within detonable limits ahead of the encroaching, highly unsteady RDW [1]. In practical RDE's with non-premixed reactant supply, it is possible that detonation waves could first be established in a homogeneous premixture with the expectation that stable detonation would then be sustained in the heterogeneously mixed fuel and oxidant. However, the thermal and/or compositional non-uniformity in the fuel refill zone are likely to cause

* Corresponding author.

E-mail addresses: huangwei.zhang@nus.edu.sg, mpezhu@nus.edu.sg (H. Zhang).

a range of unstable propagation phenomena, including quenching and initiation of multiple, new detonation waves [8,17]. Moreover, the quality of reactant mixing can also result in various RDC modes even in the same run of the RDE, i.e., under stoichiometric and off-stoichiometric conditions, or under locally premixed, non-premixed or partially premixed conditions. These phenomena are only partially understood due to the difficulty of both experimental observation and numerical simulation. Fundamental questions yet to be answered include: Can RDC proceed only through locally premixed mixtures? What fractions of the fuel are burnt by detonative and deflagrative regions of the combustor? Are locally fuel-lean or fuel-rich conditions more favorable for RDC?

Another aspect of RDC dynamics deserving of research focus is bifurcation and multiplicity of RDW's, which has been experimentally observed, and is found to be sensitive to mixture reactivity, propellant injector configuration and manifold stagnation pressure (or mass flow rate) [1]. A series of numerical simulations have been conducted to clarify the underlying mechanisms. For instance, Wang et al. [18–20] demonstrate that new RDW's are generated from shock waves surviving from the collisions between two counter-rotating detonative waves and also the interactions between the detonation and oppositely travelling shock waves. In the simulations of H₂/air RDEs by Schwer and Kailasanath [21], the new detonation wave is caused by the ignition of the unburned reactant compressed by the shock waves, which are reflected from the nozzle exit. Through modeling H₂/air RDE's with detailed chemistry and real injection nozzles, Sun et al. [22] highlight that the combustion along the contact interface between the fresh premixture and the burnt gas from the last RDW cycle may interact with reflected shocks to induce a new detonation wave. Multiple (up to four) RDW's of CH₄/air mixtures were seen in the experimental and numerical work by Frowl et al. [23]. The initiation of new RDW's is attributed to the interactions of shocks reflected from the downstream outer nozzle and the upstream refilling gas close to the head end.

Moreover, Deng et al. explore the feasibility of mode control (i.e., number and direction of RDW's) in non-premixed H₂/air RDC, through changing oxidizer mass flow rate, chamber length and exit blockage ratio [15]. They find that increased propellant reactivity leads to pre-combustion ahead of the detonation front, which may develop into a new detonation via shock wave amplification, known as the coherent energy release mechanism. More recently, Zhao and Zhang predict RDW multiplicity for an injection configuration consisting of discrete premixed jets of hydrogen and air separated by wall sections [24], and the results indicate that new RDW's evolve from chemically reactive hot spots that are enhanced by sweeping shocks. This process is observed to always follow an extended period of chaotic RDW propagation. However, the above-mentioned simulation studies, except [15], are focused on RDC in premixed propellants, and therefore bifurcation and wave multiplicity under practically relevant, non-premixed propellant injection conditions is still in need of thorough investigations.

The aims of the present paper are to study the combustion modes and mechanisms for detonation wave multiplicity in a simplified model RDE configuration with separate injection of fuel and oxidizer. A series of two-dimensional CFD simulations will be conducted, with varying global equivalence ratios and mixing levels. The effects of variation in inlet pressure and temperature are investigated, along with exploration of the sensitivity of RDC modes to the inlet configuration (specifically, the number of injection ports). In Sections 2 and 3 the computational method and the physical model are introduced. Results are presented in Section 4 and conclusions are in Section 5.

2. Governing equation and numerical method

2.1. Governing equation

The governing equations of mass, momentum, energy, and species mass fraction, together with the ideal gas equation of state, are solved. They are written as

$$\frac{\partial \rho}{\partial t} + \nabla \cdot [\rho \mathbf{u}] = 0, \quad (1)$$

$$\frac{\partial (\rho \mathbf{u})}{\partial t} + \nabla \cdot [\mathbf{u}(\rho \mathbf{u})] + \nabla p + \nabla \cdot \mathbf{T} = 0, \quad (2)$$

$$\frac{\partial (\rho \mathbf{E})}{\partial t} + \nabla \cdot [\mathbf{u}(\rho \mathbf{E})] + \nabla \cdot [\mathbf{u}p] + \nabla \cdot [\mathbf{T} \cdot \mathbf{u}] + \nabla \cdot \mathbf{q} = \dot{\omega}_T, \quad (3)$$

$$\frac{\partial (\rho Y_m)}{\partial t} + \nabla \cdot [\mathbf{u}(\rho Y_m)] + \nabla \cdot \mathbf{s}_m = \dot{\omega}_m, \quad (m = 1, \dots, M-1), \quad (4)$$

$$p = \rho RT. \quad (5)$$

Here t is time, $\nabla \cdot (\cdot)$ is divergence operator, ρ is the density, \mathbf{u} is the velocity vector, p is the pressure, Y_m is the mass fraction of m -th species and M is the total species number. Only $(M-1)$ equations are solved in Eq. (4) and the mass fraction of the inert species (e.g., nitrogen) can be recovered from $\sum_{m=1}^M Y_m = 1$. \mathbf{E} is the total energy, which is defined as $\mathbf{E} = e + |\mathbf{u}|^2/2$ with e being the specific internal energy. R in Eq. (5) is specific gas constant and is calculated from $R = R_u \sum_{m=1}^M Y_m MW_m^{-1}$. MW_m is the molar weight of m -th species and R_u is universal gas constant. \mathbf{T} in Eq. (2) is the viscous stress tensor, modeled by

$$\mathbf{T} = -2\mu \text{dev}(\mathbf{D}), \quad (6)$$

where μ is the dynamic viscosity modeled by Sutherland's law, $\mu = A_s \sqrt{T} / (1 + T_s/T)$. Here $A_s = 1.67212 \times 10^{-6} \text{ kg/m} \cdot \text{s} \cdot \sqrt{K}$ is the Sutherland coefficient, while $T_s = 170.672 \text{ K}$ is the Sutherland temperature. $\mathbf{D} \equiv [\nabla \mathbf{u} + (\nabla \mathbf{u})^T]/2$ is the deformation gradient tensor and its deviatoric component in Eq. (6), i.e., $\text{dev}(\mathbf{D})$, is defined as $\text{dev}(\mathbf{D}) \equiv \mathbf{D} - \text{tr}(\mathbf{D})\mathbf{I}/3$ with \mathbf{I} being the unit tensor. In Eq. (3), \mathbf{q} is the diffusive heat flux given by Fourier's law

$$\mathbf{q} = -k \nabla T, \quad (7)$$

with T being the temperature. Thermal conductivity, k , is calculated using the Eucken approximation [25], $k = \mu C_v (1.32 + 1.37 \cdot R/C_v)$, where C_v is the heat capacity at constant volume that is derived from $C_v = C_p - R$. Here $C_p = \sum_{m=1}^M Y_m C_{p,m}$ is the heat capacity at constant pressure, and $C_{p,m}$ is the heat capacity at constant pressure of m -th species which is estimated from JANAF polynomials [26].

In Eq. (4), $\mathbf{s}_m = -D_m \nabla (\rho Y_m)$ is the species diffusive mass flux, where $D_m = \alpha / Le_m$ is derived from the heat diffusivity, $\alpha = k / \rho C_p$, and the Lewis number which is assumed to be unity for all species (i.e., $Le_m = 1$). The net production rate of m -th species through N possible reactions is given by

$$\dot{\omega}_m = MW_m \sum_{j=1}^N \omega_{m,j}^o, \quad (8)$$

where $\omega_{m,j}^o$ is the elementary reaction rate calculated from

$$\omega_{m,j}^o = (v''_{m,j} - v'_{m,j}) \left\{ K_{fj} \prod_{m=1}^M [X_m]^{v''_{m,j}} - K_{rj} \prod_{m=1}^M [X_m]^{v'_{m,j}} \right\}. \quad (9)$$

$v''_{m,j}$ and $v'_{m,j}$ are the molar stoichiometric coefficients of the m -th species in j -th reaction, respectively. K_{fj} and K_{rj} are the forward and reverse rates of j -th reaction, respectively. $[X_m]$ is molar concentration and can be calculated from $[X_m] = \rho Y_m / MW_m$. Also, the

term $\dot{\omega}_T$ in Eq. (3) accounts for the heat release from chemical reactions and is estimated as $\dot{\omega}_T = -\sum_{m=1}^M \dot{\omega}_m \Delta h_{f,m}^0$. Here $\Delta h_{f,m}^0$ is the formation enthalpy of m -th species.

2.2. Numerical method

The governing Eqs. (1)–(4) are discretized through a cell-centered finite volume method and solved by a density-based solver, *RYrhoCentralFoam*, which is a multispecies reacting code developed in-house from the fully compressible single species OpenFOAM-based flow solver *rhoCentralFoam* [27]. This solver can simulate compressible reactive flows and performs accurate shock capturing in a collocated, polyhedral, finite-volume framework using non-oscillatory upwind-central schemes. *rhoCentralFoam* is validated by Greenshields et al. [28] and Zhang et al. [29] using various benchmark tests, including Sod's problem, a two-dimensional forward-facing step, a supersonic jet and shock-vortex interaction. It employs a central-upwind Kurganov, Noelle and Petrova (KNP) scheme [6] that has been found to be stable and efficient in shock capturing and competitive with other state-of-the-art methods such as the Roe scheme [28,29]. The reactive version, *RYrhoCentralFoam*, has been tested previously for detonative combustion [30], and shown to yield detonation cell size and propagation speed that compare well with theoretical and/or experimental values. Recently, *RYrhoCentralFoam* was used specifically for RDC problems to study instability and wave bifurcation in premixed gases [24,30], and liquid-fueled RDC [31]. A similar reactive species solver developed from *rhoCentralFoam* has also been developed by Gutierrez Marcantoni et al. [32,33] and applied to one- and two-dimensional detonations.

A second-order implicit backward method is employed for temporal discretization and the time step is about 10^{-9} s (maximum Courant number < 0.1). A second-order Godunov-type central and upwind-central scheme, i.e., KNP scheme [6], is used for the convective terms in Eq. (2). To ensure numerical stability, a van Leer limiter is adopted for the fluxes. The TVD scheme is used for discretizing the convective terms in the energy and species mass fraction equations along with a second-order central differencing scheme for the diffusion terms. Computational cost associated with the latter is minimized by an efficient Operator Splitting (OS) method that is used for both the momentum and energy equations. In the first fractional step, an explicit predictor equation is solved for the convection of conserved variables (i.e., $\rho \mathbf{u}$ and $\rho \mathbf{E}$), and in the second fractional step, an implicit corrector equation is solved for the diffusion of primitive variables (i.e., \mathbf{u} and \mathbf{E}).

The chemical source terms, $\dot{\omega}_m$ and $\dot{\omega}_T$ in Eqs. (3) and (4), are integrated with an Euler implicit method. It is known that use of detailed chemistry is important for RDE modeling, in particular in capturing unsteady combustion features such as instability of the deflagration along the contact surface between the fuel refill region and the burnt gas [22,30]. Here, a detailed hydrogen chemical mechanism with 19 reactions and 9 species [34] is used. This mechanism has been validated previously and good agreements with experimental and theoretical data are seen for ignition delay time (over a pressure range of 2–64 atm), Chapman-Jouquet detonation speed and detonation cell size [30].

It should be noted that a turbulence model is not used here. Although there have been some RDE studies which incorporate turbulence models, e.g., [35–38], they have adopted models developed for low-speed flows, e.g., Smagorinsky model [39] and WALE model [40]. Currently, our understanding of the nature of turbulence in RDE's is rather limited but it is expected that the effects of strong discontinuities and compressibility along with intense chemical heat release are likely to mean that the cascade differs, at least to some extent, from the classical Kolmogorov theory and the standard low-speed models are unlikely to be accurate [41].

Furthermore, it is essential to develop numerical schemes which on the one hand remain stable in the face of sharp discontinuities (e.g., through artificial viscosity / diffusion) while not being overly dissipative of the turbulence. Development of RDE appropriate turbulence models is an important fundamental area of study but is outside the scope of the current work.

3. Physical model

Figure 1 shows the two-dimensional rectangular domain which is used here as a simplified model of an annular RDE combustor. Because the annular RDE chamber width (typically several millimeters) is very small compared to its diameter, the computational domain of RDE can generally be “unrolled” into a two-dimensional one due to the limited radial variation within the flow field. It permits a wide range of conditions to be modeled with affordable computational effort. While it neglects three-dimensional effects such as wall boundary layers, curvature, lateral relief and vortex stretching, past two-dimensional RDC simulations [30,42,43] suggest that the main RDC characteristics can be predicted reasonably well and the results achieved are insightful in understanding physics and performance relevant to practical RDE's. This includes physically correct detonation propagation speed and flow patterns including oblique shock waves, deflagration surfaces at the interface between unreacted and burnt gases and slip lines where significant shearing and further deflagration takes place. The length (x -direction, representing combustor circumference) of the domain in Fig. 1 is 280 mm (the equivalent diameter is around 90 mm), whereas the height (y -direction) is 100 mm. These scales are close to those of laboratory-scale RDE burners, for instance the one used by Bohon et al. [11]. To obtain physically sound results on RDC with separate reactant injection, it is of great importance to use a practically relevant dimensions for the simplified model, in which reasonable timescale relations between reactant mixing and periodic RDW propagation can be reproduced.

The boundary conditions are marked in Fig. 1. The outlet has a backpressure of 1 atm and is non-reflective to avoid undesirable interference from reflected numerical pressure waves on the detonation wave and deflagration surface near the inlet of the domain. The flow exiting the domain through the outlet is supersonic at most locations and time instants, and therefore this non-reflective boundary condition is physically reasonable. The RDW's propagate continuously via periodic boundaries at the left and right sides of the domain, as indicated. Note that, in general, the propellant supply plenums and the downstream exhaust nozzle may have an influence on RDC behavior [1,44]. These effects are ignored in the present study which focuses on phenomena occurring only within the combustor.

Along the inflow boundary there are 56 (unless otherwise stated) oxidant and fuel inlet jets which are arranged according to the configuration shown in red dashed box of Fig. 1. To mimic the discrete arrangements of the reactant injection in practical RDE system, in our model, non-slip, impermeable and adiabatic walls are included between neighboring oxidant and fuel jets. A similar injector configuration was also adopted by Fujii et al. [43] for simulating RDC fueled by non-premixed ethylene and oxygen, with which they successfully achieve RDC and identify the possible mechanisms for velocity deficit relative to the ideal Chapman-Jouquet detonation wave speed.

In this work, the area ratio α (in two-dimensional case, length ratio) between wall, oxidizer and fuel is fixed at 2:2:1. The 2:1 area ratio of oxidant and fuel inlets is designed to produce unity global equivalence ratio when the oxidant is standard air (i.e., Case 1, the baseline case in our studies, tabulated in Table 1). Although variation in α may result in different RDC behaviors (e.g., variation of specific impulse, total pressure loss and velocity deficit) [21], these

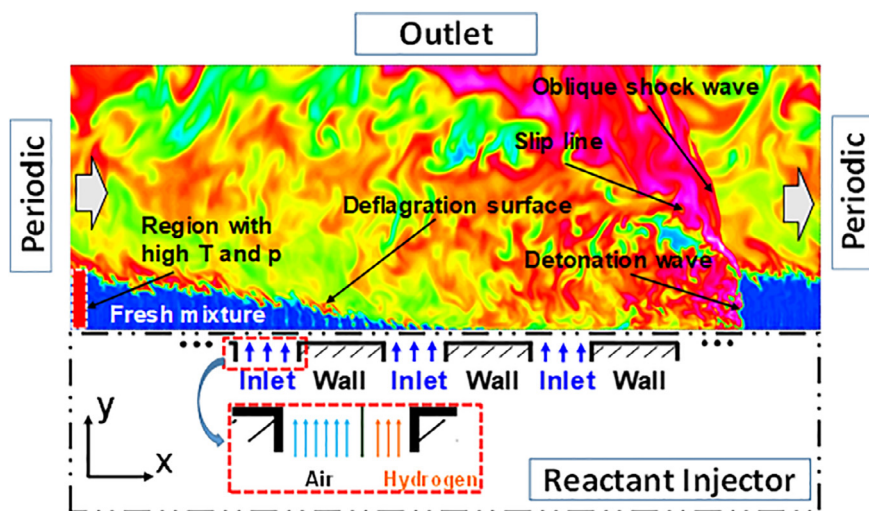


Fig. 1. Computational domain and boundary condition in two-dimensional RDC. Instantaneous temperature (200–3000 K) is shown as the background. The rectangular spot with high temperature and pressure exists only at the start of the simulation for RDW initiation. Inlet boundaries are shown schematically in the dash-dotted box and are not to scale. The grey arrows indicate the RDW propagation direction.

Table 1
Inlet species mass fraction and global equivalence ratio.

Case	Fuel ($Y_{H_2}^F$)	Oxidant ($Y_{O_2}^O : Y_{N_2}^O$)	Global equivalence ratio (ϕ_g)
1	1	0.233:0.767	1.0–1.1
2	1	0.3:0.7	0.8–0.9
3	1	0.4:0.6	0.55–0.65
4	1	0.5:0.5	0.4–0.5

effects are not studied here. Unless otherwise specified, the inlet total temperature T_0 and total pressure P_0 of both fuel and oxidant are set to 300 K and 10 atm, respectively. The flow rates of fuel and oxidizer are determined from the isentropic expansion relations between the total pressure and local pressure near the inlet [18,19,45]. Therefore, the local pressure variations near the inlet would lead to the oscillations of the fuel and oxidizer mass flow rates (see Figs. S1 and S2 in the Supplemental Material). Note that the pressure variations are mainly induced by the perturbation of local shocklets (e.g., blast wave from triple point) to the near-inlet flow field [24].

To start the RDC process, the field is initialized by an unburnt stoichiometric mixture inside a rectangular region (280 mm \times 12 mm) close to the inlet. A rectangular hot pocket (1 mm \times 12 mm, see red patch in Fig. 1) with high temperature (2000 K) and pressure (40 atm) is used to initiate a single propagating detonation wave. This RDC initiation method is different from some previous work [18,19] on RDW multiplicity, in which the multiple detonation waves are forcibly ignited by respective hot spots. Here, only a single wave is ignited and the additional detonative waves form spontaneously, as shown in detail below. Therefore, it is more relevant to practical RDE initiation, e.g., a detonative wavelet from a pre-detonator tangentially assembled to the combustor [17].

The domain in Fig. 1 is discretized with 352,800 Cartesian cells. The cell spacing in the x -direction is uniform (i.e., 0.2 mm), and in the y -direction it is continuously stretched from 0.1 mm at the inlet to 1 mm at the outlet. The stretched meshing strategies have been used in our previous work [24,30,31], and also by Fujii et al. [43]. Three-dimensional DNS of realistic RDE geometry is beyond current computing capacity. However, the present work provides sound insights into the combustion mode and wave multiplicity of RDC conditions. Sensitivity of these targets towards mesh refine-

ment is investigated in Section 4.7 through additional simulations with double the number of cells in both the x - and y -directions (1,411,200 cells in total).

Four RDC cases, Cases 1 – 4, with decreasing global equivalence ratio, ϕ_g , are studied as shown in Table 1. The time evolutions of the global equivalence ratio for these cases are shown in Fig. S3 in the Supplemental Material. It is seen in each that ϕ_g fluctuates over a small range due to fluctuations in the inlet fuel and oxidizer mass flow rates resulting from variations in the internal pressure field adjacent to the boundary. Although mass flow rates through individual inlet ports are highly variable with passing RDW's, the global mass flow rates are rather uniform. In Case 1, ϕ_g is close to stoichiometry and the value gradually decreases towards 0.4–0.5 in Case 4. The fuel is pure hydrogen in all cases, whereas the oxidant is a N_2/O_2 mixture, i.e., standard air in Case 1 and O_2 -enriched air in Cases 2, 3 and 4. Therefore, the reactivity is changed through gradually increasing the O_2 mass fraction in the oxidant stream from 30% in Case 2 to 50% in Case 4, as listed in Table 1. Note that the four cases in Table 1 have nearly the same mean global mass flow rates (see Figs. S1 and S2 in the Supplemental Material) since the injection conditions are based on inlet total pressure (10 atm for the cases in Table 1). This indicates that Cases 1 – 4 primarily test the sensitivity of the model RDE to variations in the global equivalence ratio.

4. Results and discussion

4.1. Combustion mode

Figure 2 shows instantaneous mixture fraction, flame index (FI) and heat release rate (HRR) for Case 1 when the RDW runs stably. The corresponding temperature distribution is already shown in Fig. 1. Note that the mixture fraction is computed from a transport equation which is similar to the species mass fraction equation (i.e., Eq. (4)) without the chemical source term. Similar to premixed RDC studies [30,43,45,46], the present computational modeling captures the main flow structures including the detonation and oblique shock waves, slip line and deflagration (or contact) surface (see Fig. 1). However, unlike those earlier results, the fields in the present work with separate H_2 /air injection are very inhomogeneous, which is also seen in [43]. The two reactant streams and the vitiated gas mix in the triangular fuel refill zone and the local composition is far from uniform. Since the time scale asso-

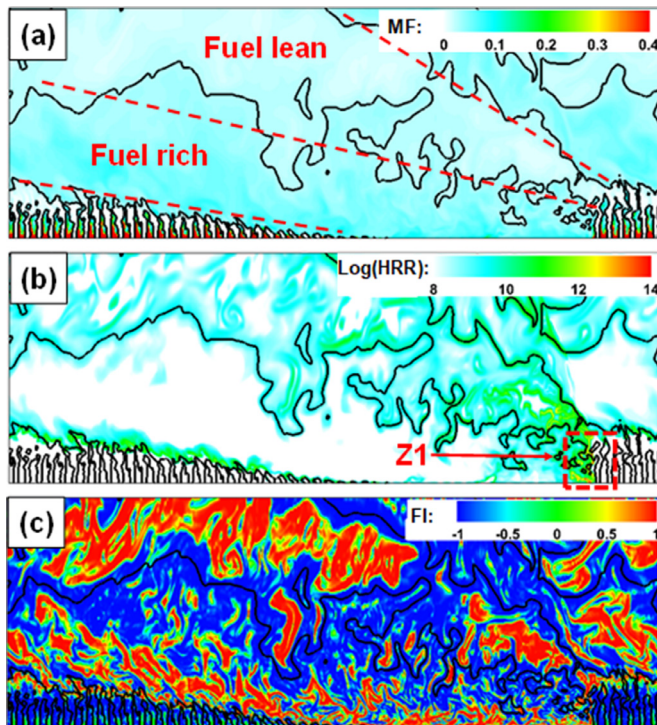


Fig. 2. Instantaneous (a) mixture fraction, (b) HRR (in $\text{J}/\text{m}^3/\text{s}$) and (c) flame index for Case 1. Black isolines: stoichiometric mixture fraction contour. Domain size: $280 \text{ mm} \times 100 \text{ mm}$.

ciated with complete fuel/oxidizer mixing is larger than both the RDW propagation time scale and the deflagration time scale, considerable unburnt reactants exist downstream of the fuel refill zone and distinct fuel-rich and fuel-lean zones are indicated in the mixture fraction field in Fig. 2(a). The fuel-rich zone, which is associated with fuel leakage, extends downstream of the detonation front and lies between the slip line and the deflagrative surface. This fuel-rich zone has limited reactions as seen by the low values of HRR. The fuel-lean zone is between the oblique shock and the slip line and some further deflagration occurs there as indicated by finite values of HRR. The presence of these spatially distributed reaction zones behind the detonation wave are supported by observations of OH^* chemiluminescence [7] and OH -PLIF images [16] from non-premixed hydrogen/air RDE experiments. Previous

simulations of premixed RDE's [30,45,47] also exhibit some fuel leakage through the triple point at the intersection of the RDW, oblique shock and deflagrative surface although, in comparison to the present non-premixed injection results, the combustion downstream occurs in a much narrower region around the slip line.

The flame index, $FI = (\nabla Y_F \cdot \nabla Y_O) / (|\nabla Y_F| |\nabla Y_O|)$, is often used to identify locations at the premixed ($FI = +1$) and non-premixed ($FI = -1$) combustion limits [48]. Here Y_F and Y_O represent the mass fractions of hydrogen and oxidizer, respectively. As shown in Fig. 2(c), even though the fuel and oxidizer are separately injected into the RDC domain, large regions of predominantly premixed combustion exist along the deflagration surface downstream of the fuel refill zone and at the detonation front. Conversely, inside the fuel refill zone, reactants are still not fully premixed, consistent with the mixture fraction distributions in Fig. 2(a). In both the fuel-lean and fuel-rich zones downstream of the triple point, both premixed and non-premixed modes are seen (although as discussed above the amount of combustion in the fuel-rich zone is quite limited).

Figure 3 shows enlarged images of mixture fraction, temperature, HRR and H_2 mass fraction around the travelling RDW, corresponding to the box region labelled "Z1" in Fig. 2(b). The locations of fuel and oxidizer inlets and walls are indicated in Fig. 3(d). A couple of interesting features are noted here. Firstly, the detonation front is highly wrinkled and does not follow along a stoichiometric contour but joins stoichiometric parcels of gas. Secondly, there is strong spatial non-uniformity of the composition along the detonation wave front, even where it follows the stoichiometric contour. This induces the discontinuous peak HRR and temperature fields shown in Fig. 3(b) and (c). This is also observed experimentally from the instantaneous OH^* chemiluminescence by Rankin et al. [7]. This non-uniformity would lead to different propagation velocities of different parts of one detonation wave [49]. Thirdly, instantaneous localized extinction can be seen along the RDW (see the arrows in Fig. 3c), which corresponds to locations with relatively low temperature and HRR in Fig. 3(b) and (c), respectively. Unburnt fuel can be transported through these extinction holes to the rear of the detonation wave as shown in Fig. 3(a) and (d), and as shown by the distributed OH^* intensity behind the RDW in Fig. 4 of [7]. This leakage mechanism has not been observed in simulations of fully premixed RDC [17,42,45,50]. In the simulations on RDC of non-premixed C_2H_4 and O_2 by Fujii et al. [43], fuel leakage is also found, but the mechanism, i.e., RDW local extinction, is not mentioned.

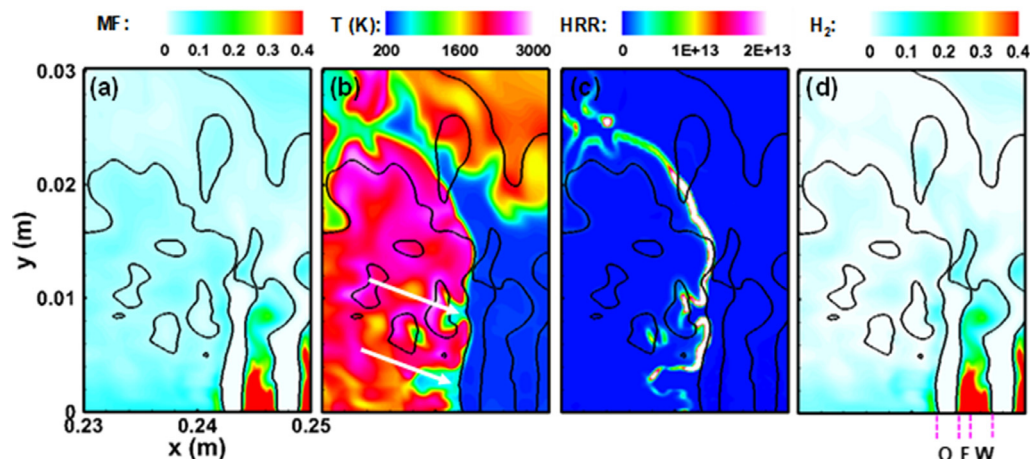


Fig. 3. Instantaneous (a) mixture fraction, (b) temperature (in K), (c) HRR (in $\text{J}/\text{m}^3/\text{s}$) and (d) H_2 mass fraction of region "Z1" in Fig. 2(b). Black isolines: stoichiometric mixture fraction contour. White arrows in Fig. 3(b) indicate localized extinction. Dashed red lines in Fig. 3(d) demarcate wall (W), oxidizer inlet (O) and fuel inlet (F). (For interpretation of the references to color in this figure legend, the reader is referred to the web version of this article.)

Table 2
Stabilized RDW properties for Cases 1–4.

Case	Detonation wave number (-)	Mean height of detonation (mm)	Propagation frequency (kHz)	Propagation Speed D (m/s)	Velocity deficit D_f (%)
1	1	16.3	5.75	1610	17.86
2	1	12.6	6.25	1750	10.71
3	3	9.7	15.93	1486	24.18
4	3	7.1	15.72	1468	25.10

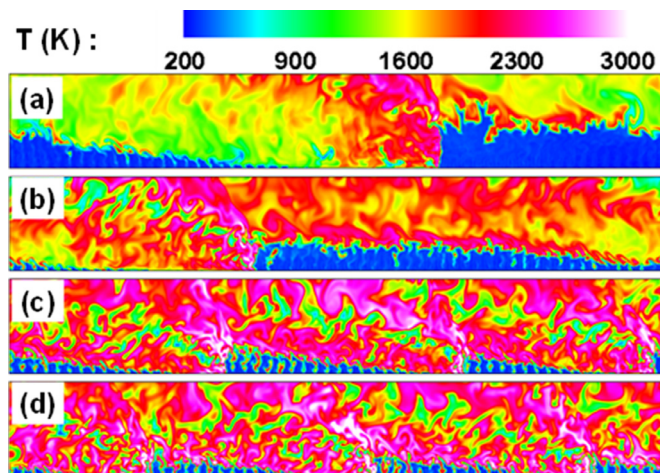


Fig. 4. Instantaneous temperature for Cases (a) 1, (b) 2, (c) 3 and (d) 4. Domain size: 280 mm \times 40 mm.

4.2. RDW multiplicity and velocity deficit

The temperature distributions for Cases 1–4 are presented in Fig. 4(a)–(d), respectively, and the quantitative information about the RDW's in the four cases are listed in Table 2. The images in Fig. 4 are taken once the rotating detonation combustion has stabilized. Only one RDW is observed in Cases 1 and 2, while Cases 3 and 4 stabilize with three RDWs. Clearly, the heights of the RDW's decrease from Case 1 to Case 4, and their time-averaged values are 16.3, 12.6, 9.7 and 7.1 mm, respectively. Here the wave height is averaged over 80 random time instants and calculated based on the y -direction distance off the inlet end where the HRR is larger than 10^{13} J/m³/s. This critical HRR value is selected based on stand-alone numerical tests of 1D H₂/air detonation propagation and was also used for identifying RDW's in our previous RDE simulations [24,30,31]. If this indicator is slightly decreased or increased, e.g., 5×10^{12} and 2×10^{13} J/m³/s, the errors in the calculated RDW heights are less than 5%. With increasing RDW number, the length (along the x -direction) of the fuel refill zone is reduced significantly with the refill lengths in Cases 3 and 4 being only one third of the corresponding lengths in Cases 1 and 2. Inside the refill zone, the temperature fields for Cases 1 and 2 are generally more homogeneous than for Cases 3 and 4 which both show more pronounced high temperature stripes which correspond to regions of vitiated gas near the boundary walls. The highly inhomogeneous nature of the refill zones for Cases 3 and 4 is the result of the shorter available reactant mixing times in those cases. The hot stripes in the fuel refill zone are characterized by significant amounts of deflagrative combustion, which has also been observed experimentally (see Fig. 4 of [7]).

The data in Table 2 shows that as the wave number increases there are decreases in both the RDW propagation speed and the velocity deficit relative to the ideal Chapman-Jouguet speed, $D_f = (D_{CJ} - D)/D_{CJ}$, although the propagation frequency increases since it accounts for all the waves that are present. Note that D_{CJ} ranges

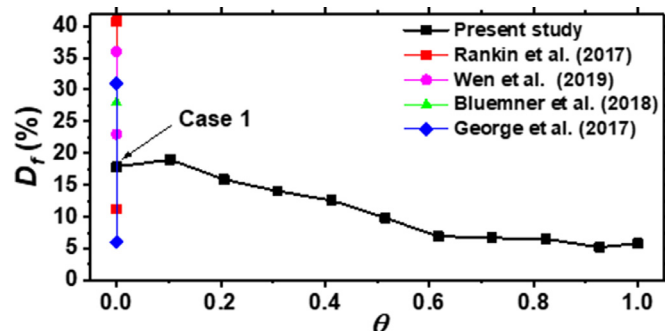


Fig. 5. Velocity deficit D_f versus reactant mixing level θ . $\theta = 0$: non-premixed; $\theta = 1$: premixed.

from 1940 to 1970 m/s for Cases 1–4 based on conditions of 1 atm and 250 K. In Case 1 (representative of fully non-premixed fuel and oxidizer), the velocity deficit is 17.86% which is comparable to the range of values reported for RDE experiments, e.g., 5%–30% by George et al. [9] and 10%–40% by Rankin et al. [7], and also RDE modeling [43]. The increasing deficit as the number of RDWs increases has also been observed experimentally [7]. It is known that there are diverse reasons for the velocity deficit in RDE's which varies with refill height, channel width and mixture reactivity [9,47,51]. In RDE's with non-premixed reactant supply, incomplete mixing of the fuel and oxidizer ahead of the propagating RDW's plays an important role in inducing this deficit.

To quantify the dependence of D_f on reactant mixing, a series of cases are considered which are variants of Case 1. We defined a mixing parameter, $\theta \equiv (1 - Y_{H_2}^F)/(1 - Y_{H_2}^{st})$, where $Y_{H_2}^F$ and $Y_{H_2}^{st}$ are the mass fractions of hydrogen in the fuel stream and a stoichiometric H₂/air mixture, respectively. Here, $Y_{H_2}^F \geq Y_{H_2}^{st}$. For $\theta = 0$ (corresponding to $Y_{H_2}^F = 1$) there is purely separated injection (i.e., non-premixed), whereas for $\theta = 1$ (corresponding to $Y_{H_2}^F = 0.0283$) there is purely premixed injection. Figure 5 shows the variation of D_f as θ is increased in increments of 0.1 by decreasing $Y_{H_2}^F$ while increasing the hydrogen fraction in the oxidizer stream $Y_{O_2}^0$ to ensure that $\phi_g \approx 1$ is maintained. The deficit is lower when there is premixing of the injected fluids and D_f ranges from about 20% for $\theta = 0$ to about 5% for $\theta = 1$. For comparison, experimentally observed velocity deficits for cases with purely separate H₂/air injection are also shown in Fig. 5 [1,7–9,52], and in general, our computed values are close to or within the range of the velocity deficits measured from various RDE experiments.

4.3. Chaotic propagation and spontaneous formation of new detonation waves

Recall that, in our simulations, one hot spot is used for ignition, which leads to one initial RDW. Generation of the additional detonation waves in Cases 3 and 4 occurs spontaneously following a period of chaotic detonation propagation. Figure 6 characterizes this transition from one to multiple detonation waves for Case 4, through the time series of H₂ mass flow rate ($\dot{m}_R = \int \rho u dA_i$) and specific impulse ($I_{sp} = \int [\rho u^2 + (p - p_b)] dA_o / g \dot{m}_R$).

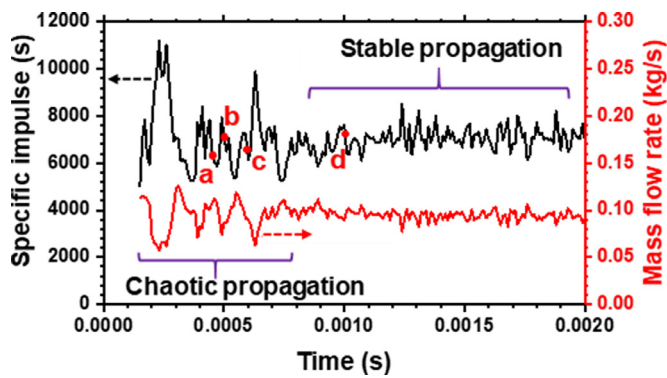


Fig. 6. Time history of specific impulse and mass flow rate for Case 4. RDW initiated at $t = 0$.

Qualitatively similar results are obtained for Case 3 (not shown). The time series are extracted once the RDW is initiated at $t = 0$. Here, A_i are the areas of all the discrete fuel inlets, A_o is the outlet area, g is gravitational acceleration and p_b is the backpressure on the outlet, which is taken as 1 atm in this work. The initial single RDW experiences chaotic propagation with considerable fluctuations of the specific impulse I_{sp} and mass flow rate \dot{m}_R . This is followed by a much more stable period with small variations of \dot{m}_R and I_{sp} , which corresponds to the stable propagation of three RDW's. The duration of the chaotic stage in Fig. 6 is approximately 0.8 ms, which is similar or slightly shorter than the similar periods of chaotic propagation prior to transition to multiple RDW's in experimental observations [9,17]. In the chaotic stage, frequent shifting between high and low heat release rates occurs, due to the highly unsteady processes of detonation extinction and re-ignition, which further cause considerable fluctuations of \dot{m}_R and I_{sp} .

Temperature and pressure fields for Case 4 corresponding to four instants during and just after the chaotic propagation stage are shown in Fig. 7. These four instants (a , b , c and d) are marked on the time series in Fig. 6. Note that instants a , b and c are in the chaotic propagation stage, whilst instant d is in stable propagation. At instant a , only one rightward propagating wave denoted $D1$ is present, which is from the initial ignition at $t = 0$. The height of the fuel refill zone is irregular and strong wrinkling is observable along the deflagration surface between burnt and unburned gases. At instant b , three new detonation waves $D2$, $D3$ and $D4$ are formed. Their respective propagation directions are various: $D2$ is left propagating, whilst $D3$ and $D4$ move rightward. Subsequently, counter-rotating $D1$ and $D2$ collide and limited fuel refilling occurs around the collision locus due to the pressure superposition. Therefore, they are attenuated quickly and ultimately degrade into two shock waves travelling along their original directions. Meanwhile, the detonation wave $D4$ gradually evolves from a localized reactive spot (see Z2 in Fig. 7a). At instant c , still in the chaotic stage, two detonative fronts, $D3$ and $D4$, co-rotate and regular triangular fuel refill zones are restored, but strong wrinkling remains on the deflagration contact surfaces. After 1.0 ms, at instant d in the stable propagation stage, three co-rotating RDW's are present. Besides $D3$ and $D4$, a new detonation wave, $D5$, is initiated after instant c at $t = 0.6$ ms. Note that the formation of $D5$ is similar to that of $D4$, i.e., from a localized reactive spot, and for brevity its generation transient is not visualized between Fig. 7(c) and (d). These unsteady phenomena are also observed in our previous simulations of chaotic RDW propagation in premixed reactant injection [24].

To further explore the mechanism of RDW formation during the chaotic stage, Fig. 8 shows the time sequences of tempera-

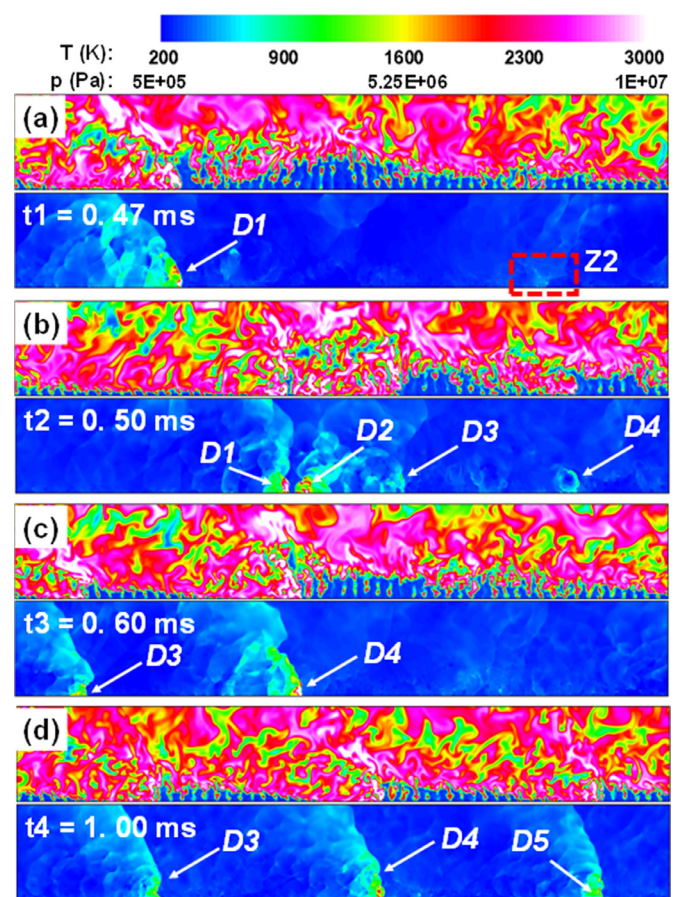


Fig. 7. Temperature (upper) and pressure (lower) fields for Case 4 at four different time instants (respectively corresponding to a , b , c and d in Fig. 6). $D1$ - $D5$ denote detonation waves.

ture, HRR and pressure in the localized area, Z2, shown in Fig. 7(a). Figures 8(a) and 7(a) correspond to the same time, i.e., $t = 0.47$ ms. At that instant, a localized hot spot with temperature about 1600 K can be seen in Fig. 8(a) (inside the elliptical circle). It is just in front of a propagating shock wave that is marked as S in the pressure distribution shown on the right. Although the high-temperature hot spot is on the stoichiometric isoline, combustion in this region is comparatively weak and no intense heat release is observed due to the relatively long ignition delay time. After the shock S sweeps through this hot spot at the next instant in Fig. 8(b), strong deflagration combustion is activated, manifest by the pronounced heat release increase along the stoichiometric isolines. However, no localized pressure increase is seen around this spot. Subsequently, a detonation wavelet D is formed in Fig. 8(c), characterized by locally high HRR and pressure. This new wave corresponds to $D4$ in Fig. 7(b), and finally evolves into a rightward propagating RDW (seen Fig. 7c). This interaction described here leads to rapid release of heat and the subsequent formation of new RDW's. Similar processes are also observed for the bifurcation into multiple RDW's in Case 3. The shock wave that may subsequently evolve into a detonation wave is formed from two possible mechanisms: (1) a blast wave originating from the triple point [24,30,53] and (2) a shock wave resulting from the collision of two counter-rotating detonation waves. The former occurs when the detonation wave impacts the contact surface between the fresh mixture and high-temperature combustion products as suggested by Houim et al. [53]. Note that the dynamic processes of new detonation wave formation occur only during the chaotic propagation stage.

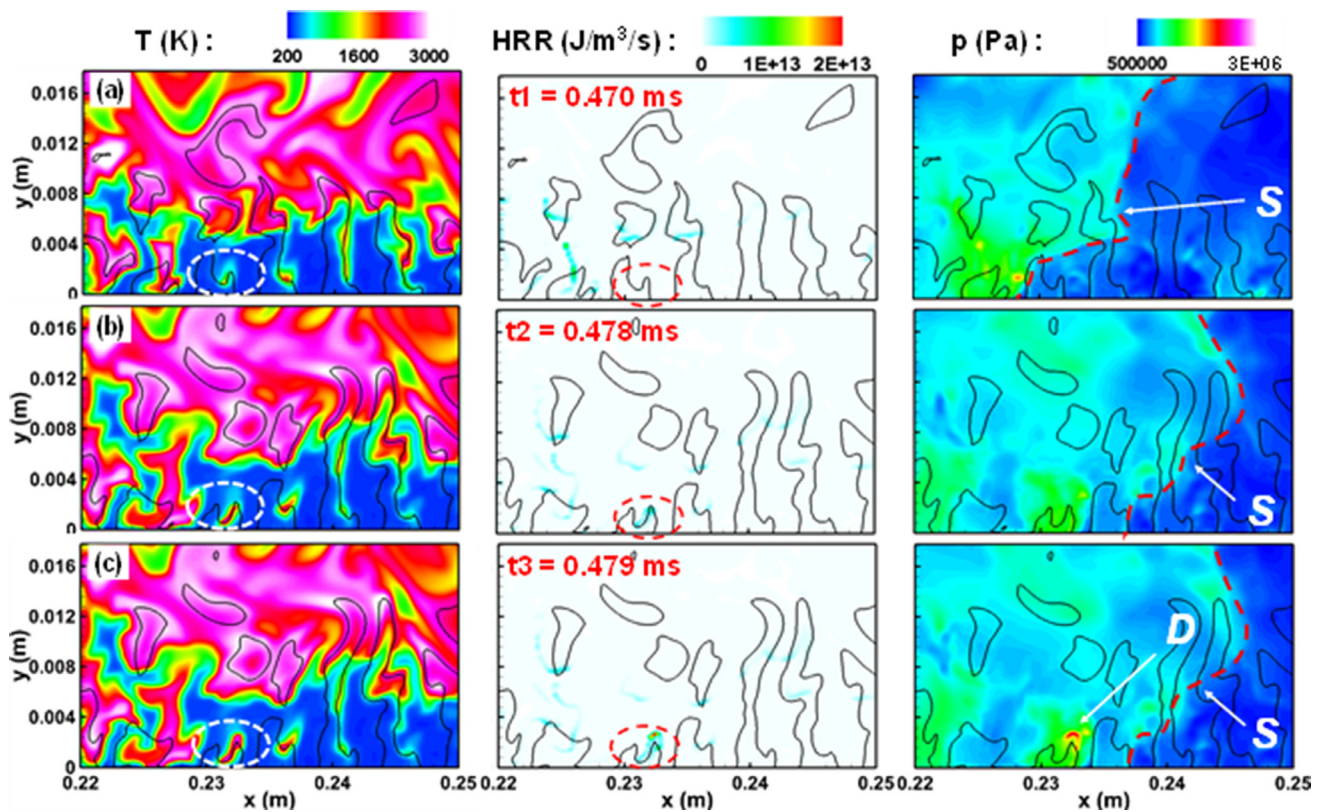


Fig. 8. Time sequences of temperature, HRR and pressure around a hot spot in zone Z2 of Fig. 7(b). First row: $t_1 = 0.47$ ms; second row: $t_2 = 0.478$ ms; third row: $t_3 = 0.479$ ms. Black isolines: stoichiometric mixture fraction contour. *D* and *S* denote detonation and shock waves, respectively.

4.4. Detonation fraction

RDE efficiency is greatest when the fuel is completely detonated rather than deflagrated. It is therefore relevant to know the fraction of fuel which is consumed through detonation in Cases 1–4 with different operating conditions. The detonation (non-detonation) fraction is calculated through volume averaging H_2 consumption rate, $\dot{\omega}_{H_2}$, conditioned on HRR being greater than (equal or less than) 10^{13} J/m³/s, which, as discussed in Section 4.2, is indicative of detonation occurring. These fractions are discussed in the contexts of combustion regime (premixed or non-premixed) and local mixture composition (lean or rich). The former is determined based on the flame index and the latter through the local mixture fraction. The detonation fractions are calculated over the entire domain from 80 random time instants with checks made over other sampling periods to ensure statistical convergence.

Figure 9 shows the detonation fractions, f_{Dt} , and non-detonation fractions (i.e., deflagration), f_{Df} , for Cases 1–4 as functions of mixture fraction. The results suggest that most H_2 is detonated under off-stoichiometric conditions, and the peak fraction of detonative H_2 is located under fuel-lean conditions. Also, the fraction of detonative H_2 in fuel-lean mixtures is higher than that in fuel-rich mixtures. This can be explained by the influences of pressure on the ignition delay (see Fig. S6 in the Supplemental Material). With increased pressure, the ignition delay of the fuel-lean mixtures is considerably reduced, but the ignition delay of the fuel-rich mixtures is increased. Meanwhile, the most reactive mixture fraction (corresponding to the mixture fraction with minimum ignition delay [54]) is leaner when the pressure is increased as shown in Fig. S6 in the Supplemental Material. Therefore, auto-ignitive combustion can occur more readily under fuel-lean mixture compositions. Note that in going from Case 1 to Case 4 the H_2 (O_2) mass flow rate is fixed (increased). This leads to increased

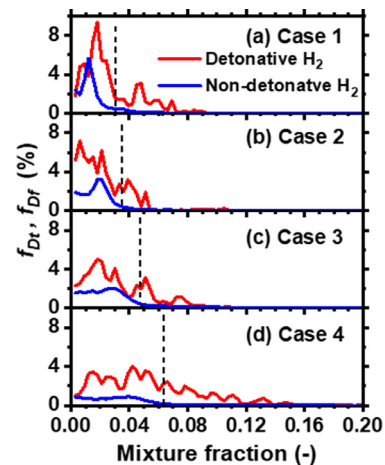


Fig. 9. Detonation and non-detonation fractions as functions of mixture fraction in Cases 1–4. The dashed lines indicate stoichiometric mixture fraction.

mixture reactivity and therefore the fractions of detonative H_2 is more distributed in Cases 3 and 4 than is the situation in Cases 1 and 2 as shown in Fig. 9. For the non-detonative burning, it is seen that most H_2 is consumed in lean mixtures for all the four cases.

Detonation and non-detonation fractions for Cases 1–4 are summarized in Table 3. Detonation accounts for about 70% in Case 1 and this number gradually increases to 80% in Case 4. This trend corresponds to a decrease in the global equivalence ratio achieved with fixed H_2 mass flow rate and increased O_2 mass flow rate from Cases 1 to 4, leading to increased mixture reactivity. Meanwhile, although f_{Dt} for Cases 3 and 4 (three RDW's) are higher than those in Cases 1 and 2 (one RDW), the RDW number does

Table 3
Detonation and non-detonation fractions for Cases 1–4.

Case	Fuel-lean (%)		Fuel-rich (%)		$FI > 0$ (%)		$FI < 0$ (%)	
	f_{Dt}	f_{Df}	f_{Dt}	f_{Df}	f_{Dt}	f_{Df}	f_{Dt}	f_{Df}
1	50.3	28.1	18.8	2.8	62.8	12.6	6.3	18.3
2	55.6	25.5	16.3	2.6	61.5	11.3	10.4	16.8
3	54.2	20.7	22.4	2.7	54.1	9.9	22.5	13.5
4	57.0	15.9	24.2	2.9	60.6	6.7	20.6	12.1

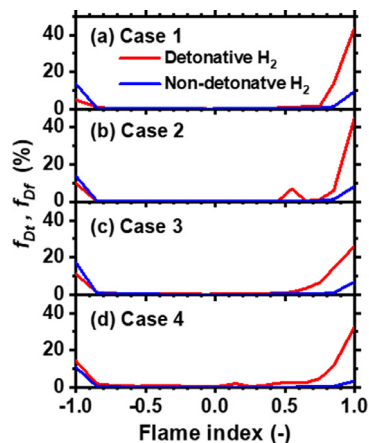


Fig. 10. Detonation and non-detonation fractions as functions of flame index for Cases 1–4.

not show striking effects on the detonation fraction, compared to the increased oxygen supply. In Table 3, it also shows that, for all the cases, a significant majority of H_2 (more than 79%) is consumed under fuel-lean conditions in either detonative or deflagrative combustion modes. Specifically, for detonation, more than 70% of H_2 is burnt under fuel-lean conditions, whereas about 28% is under fuel-rich condition. This situation is indicative of the RDW's being limited by the rate of mixing in the triangular refill zone and the detonation propagating through partially mixed reactants. Moreover, more than 80% of H_2 burns through deflagration also under fuel-lean conditions.

Figure 10 shows the detonation and non-detonation fractions as functions of flame index for Cases 1 – 4. The values of detonation and non-detonation fractions under locally premixed ($FI > 0$) and non-premixed ($FI < 0$) conditions are also listed in Table 3. The results suggest that more than 70% of the detonated H_2 is consumed in a premixed combustion mode. However, as shown in Fig. 10, the non-premixed detonation fraction is not insignificant, increasing from 9% in Case 1 to 25% in Case 4. They mainly correspond to detonation locations close to the inlet end where there is locally incomplete reactant mixing. The non-detonated fraction f_{Df} with $FI < 0$ (non-premixed) is somewhat higher than f_{Df} with $FI > 0$ (premixed) in all the cases. Moreover, from Cases 1 to 4 with increased oxygen mass flow rate, the fraction of detonative H_2 with less well-mixed reactants ($FI < 0$) increases, while the fraction of non-detonative H_2 under $FI < 0$ decreases. Note that the non-premixed deflagration mainly occurs near the slip lines, while the premixed one around the contact surfaces, as indicated by FI distribution in Fig. 2.

We now explore the sensitivity of detonation fraction to variations of inlet temperature and pressure over RDE relevant ranges. For Cases 1 and 4 only the inlet total pressure or temperature is varied, and the corresponding detonation fractions are shown in Fig. 11, which further categorizes into lean mixture fractions, and Fig. 12, which categorizes into premixed and non-premixed burning regimes. Note that the detonation fraction is calculated as the

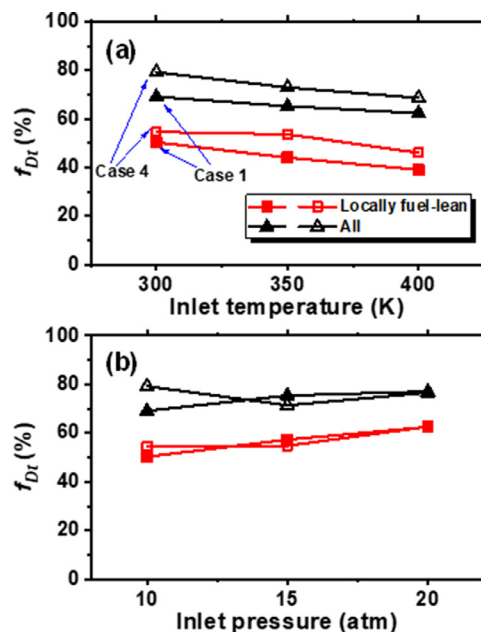


Fig. 11. Effects of (a) inlet temperature and (b) inlet pressure on detonation fraction (lean and all mixtures).

ratio of the detonated H_2 to the sum of all the reacted H_2 . As shown in Fig. 11(a), the detonated H_2 generally (denoted as all mixtures) and in lean mixtures specifically decreases as the inlet temperature increases from 300 K to 400 K. This may be because the deflagrative combustion along the contact surface is enhanced with higher inlet temperatures. Moreover, as shown in Fig. 11(b), the detonated H_2 increases, albeit not considerably, with inlet pressure. This is consistent with the trends for the variations in the most reactive mixture fraction with increasing pressure in Fig. S6 of Supplemental Material. For the detonation fractions in premixed and non-premixed conditions in Fig. 12, it is found that the detonated H_2 fraction under premixed conditions ($FI > 0$) considerably decreases as the inlet temperature increases. The opposite trend is observed for non-premixed conditions ($FI < 0$). This may be due to the fact that the mixture reactivity is increased when inlet temperature is higher, thereby leading to more H_2 detonated under non-premixed conditions. For the inlet pressure effects in Fig. 12(b), the overall trend is similar to, but not as pronounced as, that in Fig. 12(a).

4.5. Profiles of conserved and reactive scalar statistics

The mean and root-mean-square (RMS) values of mixture fraction, HRR and OH mass fraction along the detonation height direction for Cases 1 and 4 are plotted in Fig. 13. The results are obtained by volume averaging within a 2 mm zone in the x -direction centered on the moving detonation wave front and time averaging over 80 random time instants. The averaging in the x -direction has been used elsewhere as it captures the fluctuations of the highly distorted wave fronts with finite reaction zone thickness in non-premixed RDE's [7,16]. Note that the mean height of RDW's in Cases 1 and 4 are approximately 16.3 and 7.1 mm, respectively, as marked with the horizontal broken lines in Fig. 13. As seen from Fig. 13(a), for both cases, the mean mixture fractions are relatively high near the inlet end, but decay quickly downstream towards the values corresponding to global equivalence ratio. This is caused by the rapid mixing between the fuel, oxidizer and recirculating gas in the fuel refill zone. The upstream mixing is highly unsteady as confirmed by the large mixture fraction RMS there. It is emphasized

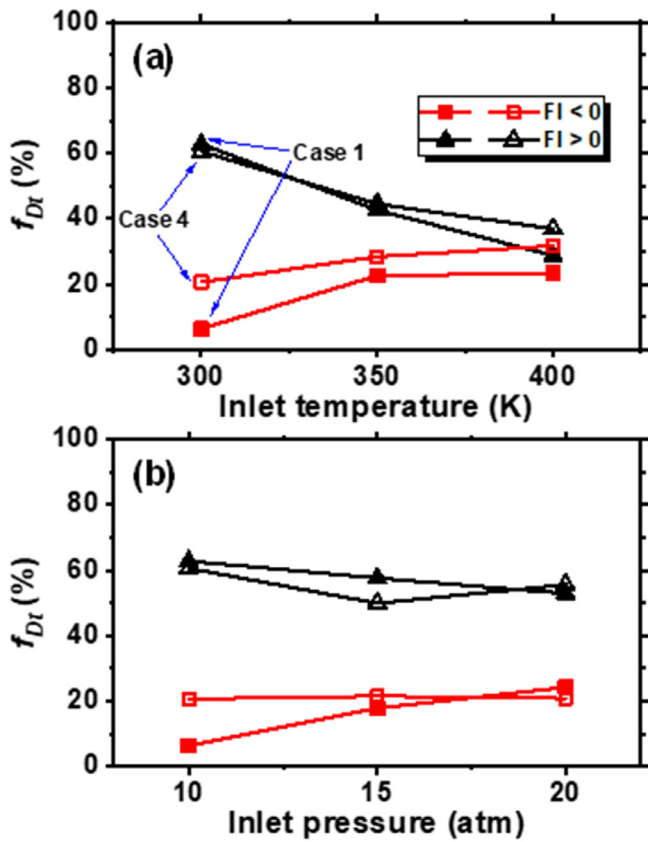


Fig. 12. Effects of (a) inlet temperature and (b) inlet pressure on detonation fraction (premixed and non-premixed conditions).

that for both cases the local compositions reach their respective global equivalence ratios at similar heights, i.e., around 7–8 mm. Therefore, for the single-waved Case 1, beyond $y = 8$ mm, the detonation wave runs in a well-mixed near-stoichiometric mixture, although the exact stoichiometric condition (marked by the blue

dashed line) is reached at around $y = 14$ mm. However, for Case 4, stoichiometry occurs at about $y = 2$ mm, which means that a majority of the detonation propagates through imperfectly mixed (greater than global equivalence ratio) and off-stoichiometric gas.

Figure 13(b) shows the distributions of mean and RMS values of HRR along the detonation wave front. For Case 1, mean HRR gradually increases until $y = 6$ mm and then levels off at about 10^{13} J/m³/s over the remainder of the detonation height corresponding to near-stoichiometric conditions. However, for Case 4, HRR increases rapidly towards the peak value at $y = 2$ mm, close to the stoichiometric height, and then gradually decreases over the remainder of the detonation wave. Beyond their respective detonation heights, HRR is reduced in both cases. The relatively flat profile of HRR from the single-waved Case 1 may be caused by the better reactant mixing in the significantly larger fuel refill zone. Additionally, generally higher HRR in Case 4 is probably due to the increased mass flow rate of oxygen in the oxidant injection. The non-uniform distribution of HRR along the RDW height is also observable from the OH* chemiluminescence images in [7] (Note that OH* chemiluminescence is qualitatively related to HRR [55,56]). Moreover, the RMS values of HRR in both cases are much larger than the respective means, indicating the strong unsteadiness of the detonative combustion due to the reactant non-uniformity in the fuel refill zone. This local non-uniformity exists in both x - and y -direction, as seen in Fig. 3.

The OH mass fraction along the RDW height is shown in Fig. 13(c). For Case 1, both mean and RMS values slowly increase and when the height is larger than 8 mm, they are almost constant due to the locally near-stoichiometric mixtures. In Case 4, OH concentration within the RDW height is much larger than that of Case 1. This may be because in Case 4 the mixtures near the detonation wave are off-stoichiometric, and more oxygen supply leads to higher mixture reactivity. Moreover, OH concentration keeps rising beyond the detonation height (7.1 mm), peaking at $y = 12$ mm before decreasing again. These OH radicals in Case 4 are generated from the deflagrative combustion near the triple point. This has been confirmed by examining the 2D OH contours for Case 4 (not shown here), and is also observed in the OH-PLIF images by

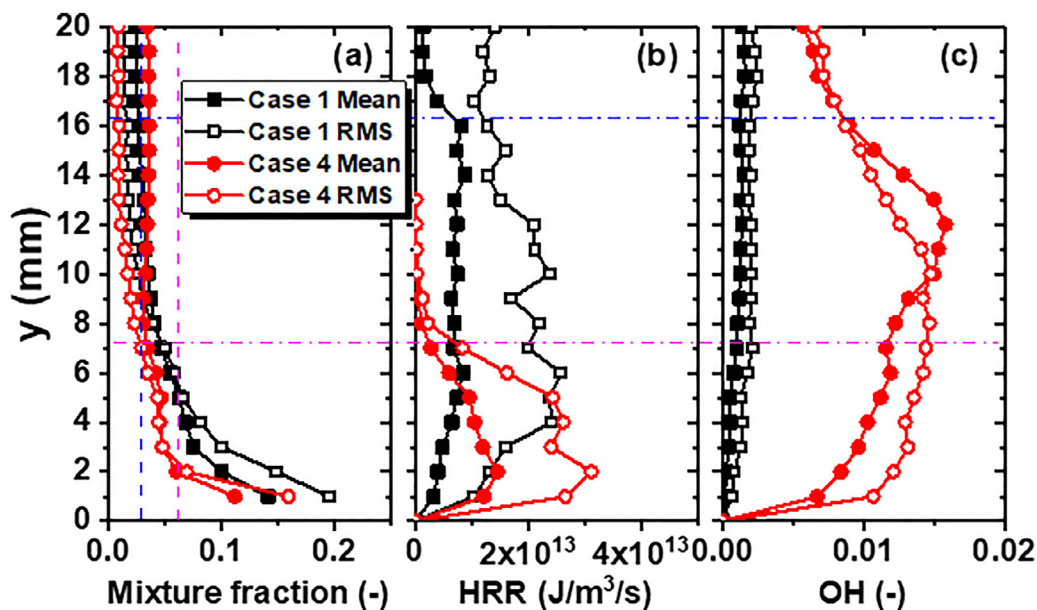


Fig. 13. Profiles of mean and root-mean-square values of (a) mixture fraction, (b) heat release rate and (c) OH mass fraction for Cases 1 and 4. Blue and magenta dashed lines: stoichiometry for Cases 1 and 4, respectively. Blue and magenta dash-dotted lines: mean detonation height for Cases 1 and 4, respectively. (For interpretation of the references to color in this figure legend, the reader is referred to the web version of this article.)

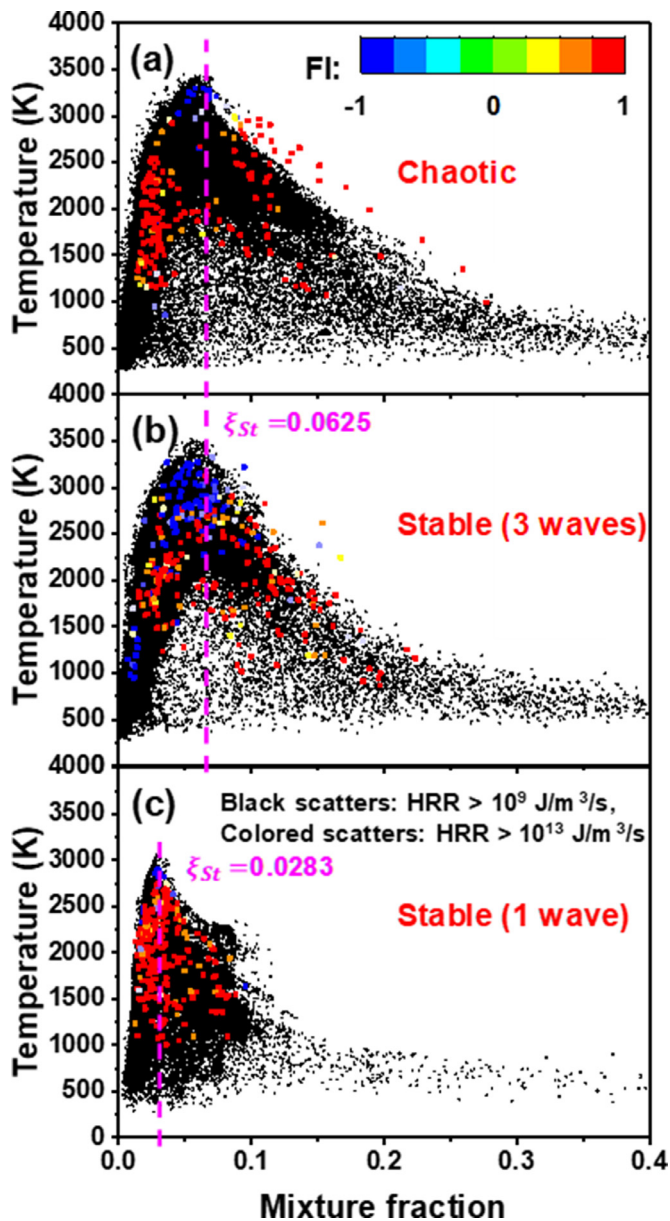


Fig. 14. Scatter plots of temperature versus mixture fraction for (a,b) Case 4 and (c) Case 1. These scatters are collected from the whole domain at one instant. Dashed lines: stoichiometry. Black points represent deflagration and detonation and the color points (scaled by flame index) represent detonation only.

Chacon and Gamba [16]. In this sense, HRR or OH^* chemiluminescence is a better indicator for RDW identification.

4.6. Detonation and deflagration flame structure

Figure 14 shows scatter plots of temperature versus mixture fraction for Cases 1 and 4. For Case 4 results are presented during both the chaotic and stable propagation stages in Fig. 14(a) and (b), respectively. The black data points correspond to locations with $\text{HRR} > 10^9 \text{ J/m}^3/\text{s}$, which is indicative of zones with either detonation or deflagration. More than 99% of the hydrogen is found to be reacted with $\text{HRR} > 10^9 \text{ J/m}^3/\text{s}$. The colored points are for locations with $\text{HRR} > 10^{13} \text{ J/m}^3/\text{s}$, which is indicative of detonation only and the coloring represents the flame index. The computed range of mixture fractions which can lead to detonation in Case 1 is 0.01–0.1, which is quite close to the detonable range of 0.015–0.09 suggested by Glassman [57] and narrower than the flammable

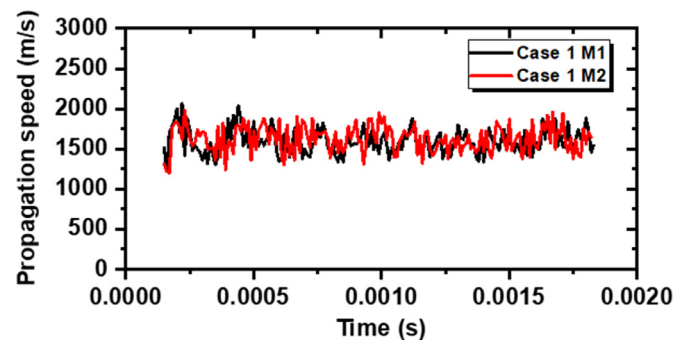


Fig. 15. Time history of detonation propagation speed for two meshes, M1 and M2, for Case 1.

range of 0.003–0.164 [57]. In Case 4, these ranges are extended due to additional oxygen addition in the oxidizer.

In the chaotic propagation stage for Case 4 shown in Fig. 14(a), two branches are discernible. The upper branch corresponds to detonation, while the lower branch represents either developing detonative or intense deflagrative combustion. It is apparent that the detonation zone is dominated by a premixed combustion mode (red dots), although there are some non-premixed, high temperature points (at about 3300 K) around the stoichiometric region the upper branch as well. These non-premixed samples come from the root of the detonation front close to the reactant inlets, where strong non-uniformity exists due to incomplete mixing.

In the stable propagation stage for Case 4 in Fig. 14(b), the detonation zone temperature is more scattered; even near stoichiometry it ranges from about 1800 K to 3000 K. This is characteristic of frequent localized extinction along the stably propagating RDW's. Recall that in Case 4 there are three RDW's, and that these have shorter fuel refill zones and shorter mixing times compared to the single RDW cases. As such, considerable numbers of locations have non-premixed or partially premixed combustion in Fig. 14(b). Conversely, in Case 1 with single RDW in Fig. 14(c), most of the detonation proceeds under premixed mode except for a few non-premixed points at the root.

4.7. Sensitivity to mesh resolution

To clarify the effect of grid resolution on the major features of the flows, simulations of Case 1 (with a single wave) and Case 4 (with three waves) are repeated with a finer mesh. As mentioned in Section 3, the cell numbers in both x - and y -directions are doubled. For brevity, hereafter the original mesh used for the preceding analysis is referred to as M1, and the refined mesh is referred to as M2.

Figure 15 shows the time history of detonation propagation speed for Case 1 using both meshes. Here the detonation propagation speed is estimated based on two adjacent time instants (i.e., $\Delta t = 1 \times 10^{-5} \text{ s}$). Since the detonation wave is highly wrinkled as seen in Fig. 3, the speed is calculated using the wave position defined as the point of maximum heat release rate. The mean RDW speeds for M1 and M2 are quite similar at 1610 m/s and 1627 m/s, respectively, and the RMS are very close at 9.8% and 10%, respectively. Furthermore, both meshes lead to a single right-propagating RDW. Similar low sensitivity of mean wave speed and wave number to the grid is reported in our recent modeling of premixed RDW's [24]. Figure 15 shows instantaneous, stochastic differences in RDW propagation speed for the two meshes, which is to be expected due to local resolution differences in the solved fields (even if numerical error could be eliminated). For example, mesh M2 produces greater wrinkling and local propagation of the deflagration surface, and smaller scale local flow structures between

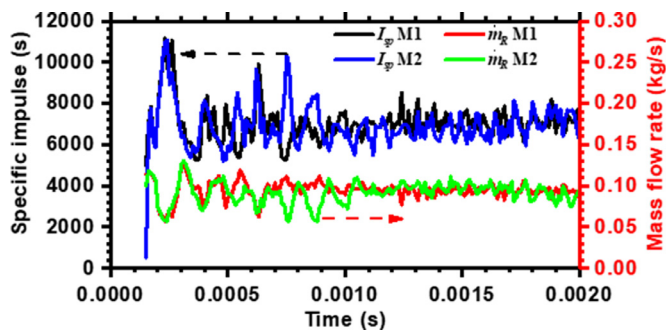


Fig. 16. Time history of specific impulse and fuel mass flow rate with two meshes, M1 and M2, for Case 4.

Table 4
Detonation and non-detonation fractions for Cases 1 and 4. Results from mesh M2.

Case	Fuel-lean (%)		Fuel-rich (%)		$FI > 0$ (%)		$FI < 0$ (%)	
	f_{Dt}	f_{Df}	f_{Dt}	f_{Df}	f_{Dt}	f_{Df}	f_{Dt}	f_{Df}
1	53.7	24.2	19.4	2.7	64.2	9.5	8.0	18.3
4	55.1	19.4	22.3	3.2	58.3	8.8	19.1	13.8

the fuel and oxidizer streams in the refill zone and between gases along the slip plane (not shown for brevity). However, the results shown in Fig. 15 (and below) indicate that these local resolution differences have only minor effects on major flow characteristics including wave speed and multiplicity. For further information the interested reader is referred to Oran and co-workers [58,59] who have investigated the influence of local resolution induced stochasticity in their simulations of Deflagration-to-Detonation Transition (DDT).

To elaborate the effects of mesh resolutions on RDC with chaotic propagation and bifurcation, Fig. 16 compares the time history of specific impulse I_{sp} and fuel mass flow rate \dot{m}_R for meshes M1 and M2 for Case 4. Both meshes have a chaotic propagation period, with considerable fluctuations of I_{sp} and \dot{m}_R and spontaneous formation of new RDW's (see Section 4.3). This is followed by the stable propagation period in which three, right-propagating RDW's are present for both meshes. The magnitude of the fluctuations in both the chaotic and stable periods is very similar for the two meshes. The duration of the chaotic stage differs slightly, estimated to be 0.8 ms for M1 and 1.1 ms for M2. The detailed analysis in Section 4.3 of the mechanisms leading to the formation of new waves (including counter-rotation and flame-shock interactions) has been repeated for the finer mesh M2 but is not shown here. The dynamics are very similar although there are stochastic differences in the precise time and place that each phenomenon occurs due to variations in resolution of local features. An accumulation of these local differences between the two meshes leads to an overall difference in the duration of the chaotic propagation period but no change in the conclusions about how new waves are formed or their number.

Table 4 gives the detonation and non-detonation fractions, f_{Dt} and f_{Df} , grouped by local composition (lean, rich) and combustion modes (premixed, non-premixed) using mesh M2 for Cases 1 and 4. A comparison to the same set of results for mesh M1 shown earlier in Table 3, reveals only very minor differences. For example, the fraction of detonated H_2 under fuel-lean conditions was about 70% for M1, and here it is about 71% for M2.

Overall, the results presented in this section indicate that although there is some local sensitivity to grid resolution, the major features of the flow (including wave number, propagation direction, mechanisms of bifurcation, specific impulse, fuel mass flow rate and detonation fraction) are relatively insensitive.

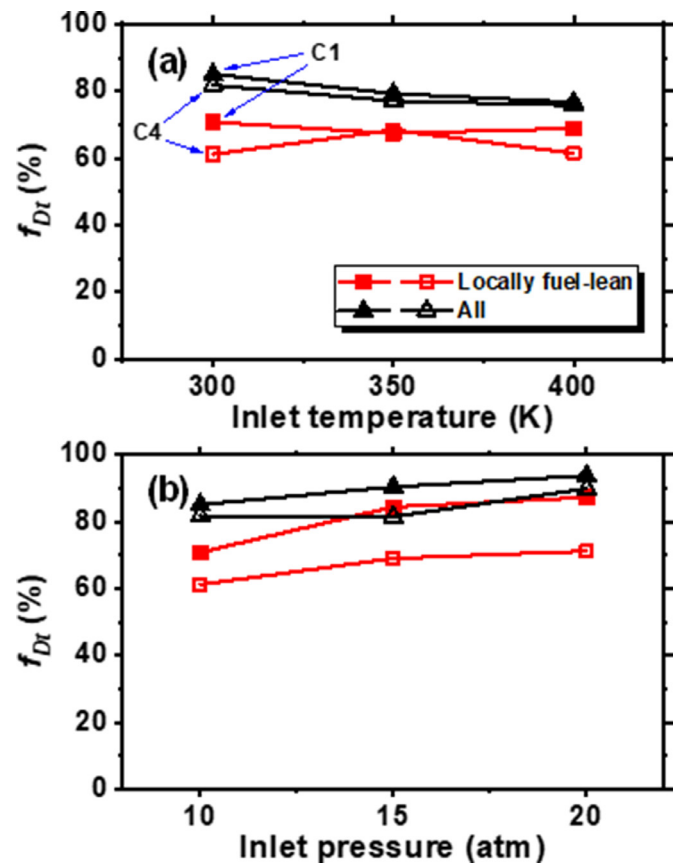


Fig. 17. Detonation fraction (fuel-lean and all the mixtures) as a function of (a) inlet temperature and (b) inlet pressure for Cases 1 and 4. The injection orifice number is 112. C1: the same inlet temperature and pressure as Case 1, C4: the same inlet temperature and pressure as Case 4.

4.8. Sensitivity to inlet configuration

Up to this point, all simulations are for an RDE with 56 injectors. In this section the sensitivity of RDC behavior to a doubling of the injector number to 112 is briefly examined. This has important practical implications as the injector configuration has an effect on the amount of mixing in the refill zone. Note that the Cases with 112 injectors have the same computational domain as the cases with 56 injectors shown in Fig. 1 and the area ratio α (in the two-dimensional case, length ratio) between wall, oxidizer and fuel is also fixed at 2:2:1 by halving the respective lengths.

The effects of inlet pressure and temperature on detonation fraction with 112 injection orifices are shown in Figs. 17 and 18. In general, the trend of detonation fractions with 112 injection orifices is similar to that with 56 injection orifices for variable inlet pressures and temperatures. For instance, the detonation fraction in all mixtures decreases with inlet temperature, whilst it increases with inlet pressure. However, there are still some differences. For instance, the detonation fraction in non-premixed conditions increases with inlet pressure, while it decreases with 56 orifices. Moreover, by comparing the detonation fractions in premixed conditions in Fig. 18 with those in Fig. 12, we see that at the same inlet pressure or temperature the detonation fraction under premixed conditions with 112 orifices is generally higher than that with 56 orifices. This is because the reactant mixing in the refill zone is enhanced, which is consistent with the increased detonation propagation speed with higher injector number (see Tables S1 and S2 and Figs. S4 and S5 in Supplemental Material).

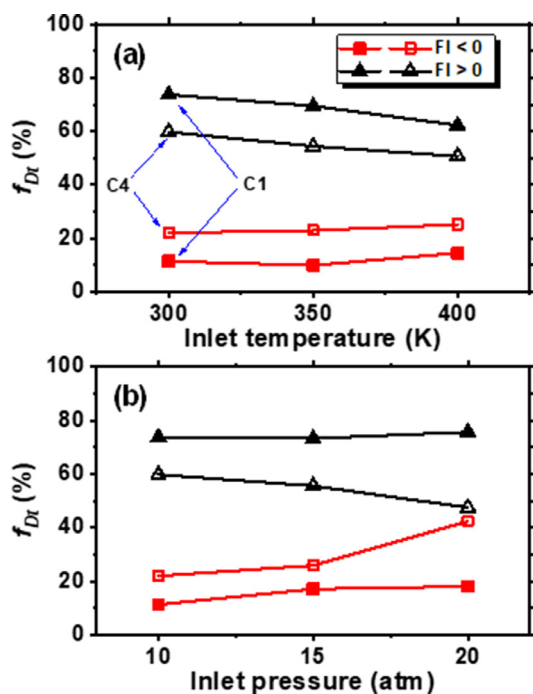


Fig. 18. Detonation fraction (premixed/non-premixed) as a function of (a) temperature and (b) pressure for Cases 1 and 4. The injection orifice number is 112. Implications of C1 and C4 same as that in Fig. 17.

5. Conclusions

Simulations of two-dimensional rotating denative combustion with separately injected hydrogen and air are performed using detailed chemical kinetics in this work. Four cases are investigated with various fuel and oxidant compositions and the emphasis is laid on their influences on combustion mode and detonation wave bifurcation.

The results show that the reactant in the refill zone is highly imhomogeneous due to the insufficient mixing before the detonation wave arrives. Also, fuel-rich and fuel-lean zones exist beyond the refill zone. Deflagrative combustion proceeds in the fuel-lean zone, whilst limited reaction occurs in the fuel-rich zone.

With increased oxygen concentration in the oxidant stream, the detonation wave number increases from one to three in the simulated cases. A transient analysis reveals that, in cases with multiple waves, new waves are spawned during a chaotic propagation stage and result from the interactions between the highly reactive hot pockets and travelling shocks. The detonation propagation speed deficits from the simulation cases vary between 10% and 25%, which is observed to decrease with increased reactant mixing level.

The statistics of hydrogen consumption rate show that limited amounts (less than 3.7%) are detonated or deflagrated close to the stoichiometric condition. Over 70% of the detonated H_2 is consumed under fuel-lean conditions, whilst over 80% of non-detonated hydrogen is reacted under fuel-lean conditions. This is mainly because the ignition delay time of fuel-lean (fuel-rich) mixtures is considerably reduced (increased) with elevated pressure. The remaining fractions of hydrogen are detonated or deflagrated under fuel-rich condition. Meanwhile, both the deflagration and detonation zones are found to be dominated by a premixed combustion mode. At least 70% of the detonated H_2 is consumed within a premixed combustion mode. The fraction of the non-detonated H_2 with negative flame index is slightly higher than that with positive flame index in all the cases. Furthermore, in-

creasing the inlet temperature (inlet pressure) generally decreases (increases) fuel detonation fraction and RDW propagation speed. Higher injection orifice number can significantly improve the stability of detonation propagation, characterized by higher RDW propagation speed and detonation fraction. This is because the mixing between the fuel and oxidizer is enhanced with increased injection orifice number.

Moreover, the statistics of conserved and reactive scalars along the detonation wave front indicate that the reactant mixing has significant influences on the unsteadiness of the detonative combustion and detonation wave propagation. The trends in heat release and OH mass fraction from the present simulations are qualitatively similar to those from RDE measurements.

Our results also demonstrate that the range of detonable mixture fraction is narrower than that for deflagration, and would be extended with increased mass flow rate of oxygen in the oxidant stream. In addition, the detonation and developing detonation or intense deflagration are discerned with two branches in the chaotic stage. Mesh sensitivity analysis is performed and it is shown that the mesh resolution does not influence the predictions of chaotic propagation, RDW number / direction, and fractions of detonated fuels.

Declaration of Competing Interest

None.

Acknowledgment

This work used the computational resources in National Supercomputing Center, Singapore (<https://www.nscg.sg/>), and is partially supported by USyd–NUS Partnership Collaboration Awards.

Supplementary materials

Supplementary material associated with this article can be found, in the online version, at doi:[10.1016/j.combustflame.2020.11.001](https://doi.org/10.1016/j.combustflame.2020.11.001).

References

- [1] V. Anand, E. Gutmark, Rotating detonation combustors and their similarities to rocket instabilities, *Prog. Energy Combust. Sci.* 73 (2019) 182–234.
- [2] P. Wolański, Detonative propulsion, *Proc. Combust. Inst.* 34 (2013) 125–158.
- [3] K. Kailasanath, Recent developments in the research on rotating-detonation-wave engines, 55th AIAA Aerospace Sciences Meeting (2017), p. 0784.
- [4] E.M.B. Lu, K. Frank, Rotating detonation wave propulsion: experimental challenges, modeling, and engine concepts., *J. Propuls. Power* 4 (2014) 464–470.
- [5] R. Zhou, D. Wu, J. Wang, Progress of continuously rotating detonation engines, *Chin. J. Aeronaut.* 29 (2016) 15–29.
- [6] B.V. Voitsekhozhkii, V.V. Mitrofanov, M.E. Topchiyan, Structure of the detonation front in gases (survey), *Combust. Explos. Shock Waves* 5 (1969) 267–273.
- [7] B.A. Rankin, D.R. Richardson, A.W. Caswell, A.G. Naples, J.L. Hoke, F.R. Schauer, Chemiluminescence imaging of an optically accessible non-premixed rotating detonation engine, *Combust. Flame* 176 (2017) 12–22.
- [8] H. Wen, Q. Xie, B. Wang, Propagation behaviors of rotating detonation in an obround combustor, *Combust. Flame* 210 (2019) 389–398.
- [9] A. St. George, R. Driscoll, V. Anand, E. Gutmark, On the existence and multiplicity of rotating detonations, *Proc. Combust. Inst.* 36 (2017) 2691–2698.
- [10] F.A. Bykovskii, S.A. Zhdan, E.F. Vedernikov, Continuous spin detonations, *J. Propuls. Power* 22 (2006) 1204–1216.
- [11] M.D. Bohon, R. Bluemner, C.O. Paschereit, E.J. Gutmark, Measuring rotating detonation combustion using cross-correlation, *Flow Turbul. Combust.* 103 (2019) 271–292.
- [12] R.M. Russo, P.I. King, F.R. Schauer, L.M. Thomas, Characterization of pressure rise across a continuous detonation engine, 47th AIAA/ASME/SAE/ASEE Joint Propulsion Conference & Exhibit, AIAA, 2011 2011-6046.
- [13] A.C. St. George, Development and testing of pulsed and rotating detonation combustors, University of Cincinnati, 2016.
- [14] Q. Xie, H. Wen, W. Li, Z. Ji, B. Wang, P. Wolanski, Analysis of operating diagram for H₂/Air rotating detonation combustors under lean fuel condition, *Energy* 151 (2018) 408–419.
- [15] L. Deng, H. Ma, C. Xu, X. Liu, C. Zhou, The feasibility of mode control in rotating detonation engine, *Appl. Therm. Eng.* 129 (2018) 1538–1550.

- [16] F. Chacon, M. Gamba, OH PLIF visualization of an optically accessible rotating detonation combustor, *AIAA Propulsion Energy Forum* (2019), p. 4217.
- [17] V. Anand, A. St. George, J. Jodele, E. Knight, E. Gutmark, Black-box modeling of rotating detonation combustors and their injector plena coupling, *AIAA J.* (2019) 1–12.
- [18] S. Yao, J. Wang, Multiple ignitions and the stability of rotating detonation waves, *Appl. Therm. Eng.* 108 (2016) 927–936.
- [19] S. Yao, M. Liu, J. Wang, Numerical investigation of spontaneous formation of multiple detonation wave fronts in rotating detonation engine, *Combust. Sci. Technol.* 187 (2015) 1867–1878.
- [20] Z. Xia, X. Tang, M. Luan, S. Zhang, Z. Ma, J. Wang, Numerical investigation of two-wave collision and wave structure evolution of rotating detonation engine with hollow combustor, *Int. J. Hydrogen Energy* 43 (2018) 21582–21591.
- [21] D. Schwer, K. Kailasanath, Feedback into mixture plenums in rotating detonation engines, 50th AIAA Aerospace Sciences Meeting Including the New Horizons Forum and Aerospace Exposition (2012), p. 617.
- [22] J. Sun, J. Zhou, S. Liu, Z. Lin, J. Cai, Effects of injection nozzle exit width on rotating detonation engine, *Acta Astronaut.* 140 (2017) 388–401.
- [23] S.M. Frolow, V.S. Aksenov, V.S. Ivanov, S.N. Medvedev, I.O. Shamshin, *Flow structure in rotating detonation engine with separate supply of fuel and oxidizer: experiment and CFD, Detonation Control for Propulsion*, Springer (2018), pp. 39–59.
- [24] M. Zhao, H. Zhang, Origin and chaotic propagation of multiple rotating detonation waves in hydrogen/air mixtures, *Fuel* 275 (2020) 117986.
- [25] B.E. Poling, J.M. Prausnitz, J.P. O'Connell, *The Properties of Gases and Liquids*, McGraw-Hill, New York, 2001.
- [26] B.J. McBride, *Coefficients for Calculating Thermodynamic and Transport Properties of Individual Species*, National Aeronautics and Space Administration, Office of Management, 1993 Scientific and Technical Information Program.
- [27] H. Jasak, *Error analysis and estimation for the finite volume method with applications to fluid flows*, Imperial College London (1996).
- [28] C.J. Greenshields, H.G. Weller, L. Gasparini, J.M. Reese, Implementation of semi-discrete, non-staggered central schemes in a colocated, polyhedral, finite volume framework, for high-speed viscous flows, *Int. J. Numer. Methods Fluids* 63 (2010) 1–21.
- [29] H. Zhang, M. Zhao, Z. Huang, Large eddy simulation of turbulent supersonic hydrogen flames with OpenFOAM, *Fuel* 282 (2020) 118812.
- [30] M. Zhao, J.-M. Li, C.J. Teo, B.C. Khoo, H. Zhang, Effects of variable total pressures on instability and extinction of rotating detonation combustion, *Flow Turbul. Combust.* 104 (2020) 261–290.
- [31] M. Zhao, H. Zhang, Modelling rotating detonative combustion fueled by partially pre-vaporized n-Heptane sprays, *Phys. Fluids* (2020) Submitted for publication.
- [32] L.F. Gutiérrez Marcantoni, J. Tamagno, S. Elaskar, rhoCentralRfFoam: an OpenFOAM solver for high speed chemically active flows – simulation of planar detonations, *Comput. Phys. Commun.* 219 (2017) 209–222.
- [33] L.F. Gutiérrez Marcantoni, J. Tamagno, S. Elaskar, Two-dimensional numerical simulations of detonation cellular structures in H₂O₂/Ar mixtures with OpenFOAM®, *Int. J. Hydrogen Energy* 42 (2017) 26102–26113.
- [34] J.-Y. Choi, I.-S. Jeung, Y. Yoon, Computational fluid dynamics algorithms for unsteady shock-induced combustion, part 2: comparison, *AIAA J.* 38 (2000) 1188–1195.
- [35] P.A. Cocks, A.T. Holley, B.A. Rankin, High fidelity simulations of a non-premixed rotating detonation engine, 54th AIAA Aerospace Sciences Meeting (2016), pp. 1–18.
- [36] S. Matsuyama, K. Iwata, Y. Nunome, H. Tanno, T. Mizukaki, M. Kojima, H. Kawashima, Large-eddy simulation of rotating detonation with a non-premixed CH₄/O₂ injection, *AIAA Scitech Forum* (2020), p. 1174.
- [37] M. Zhao, H. Zhang, Large eddy simulation of non-reacting flow and mixing fields in a rotating detonation engine, *Fuel* 280 (2020) 118534.
- [38] P. Pal, C. Xu, G. Kumar, S.A. Drennan, B.A. Rankin, S. Som, Large-eddy simulations and mode analysis of ethylene/air combustion in a non-premixed rotating detonation engine, *AIAA Propulsion Energy Forum* (2020), p. 3876.
- [39] M. Germano, U. Piomelli, P. Moin, W.H. Cabot, A dynamic subgrid-scale eddy viscosity model, *Phys. Fluids A Fluid Dyn.* 3 (1991) 1760–1765.
- [40] F. Nicoud, F. Ducros, Subgrid-scale stress modelling based on the square of the velocity gradient tensor, *Flow Turbul. Combust.* 62 (1999) 183–200.
- [41] Y. Mahmoudi, K. Mazaheri, S. Parvar, Hydrodynamic instabilities and transverse waves in propagation mechanism of gaseous detonations, *Acta Astronaut.* 91 (2013) 263–282.
- [42] D. Schwer, K. Kailasanath, Numerical investigation of the physics of rotating-detonation-engines, *Proc. Combust. Inst.* 33 (2011) 2195–2202.
- [43] J. Fujii, Y. Kumazawa, A. Matsuo, S. Nakagami, K. Matsuoaka, J. Kasahara, Numerical investigation on detonation velocity in rotating detonation engine chamber, *Proc. Combust. Inst.* 36 (2017) 2665–2672.
- [44] N. Jourdain, N. Tsuboi, K. Ozawa, T. Kojima, A.K. Hayashi, Three-dimensional numerical thrust performance analysis of hydrogen fuel mixture rotating detonation engine with aerospike nozzle, *Proc. Combust. Inst.* 37 (2019) 3443–3451.
- [45] M. Hishida, T. Fujiwara, P. Wolanski, Fundamentals of rotating detonations, *Shock Waves* 19 (2009) 1–10.
- [46] D. Schwer, K. Kailasanath, Fluid dynamics of rotating detonation engines with hydrogen and hydrocarbon fuels, *Proc. Combust. Inst.* 34 (2013) 1991–1998.
- [47] V.R. Katta, K.Y. Cho, J.L. Hoke, J.R. Codoni, F.R. Schauer, W.M. Roquemore, Effect of increasing channel width on the structure of rotating detonation wave, *Proc. Combust. Inst.* 37 (2019) 3575–3583.
- [48] H. Yamashita, M. Shimada, T. Takeno, A numerical study on flame stability at the transition point of jet diffusion flames, *Symp. (Int.) Combust., Elsevier* (1996), pp. 27–34.
- [49] L.R. Boeck, F.M. Berger, J. Hasslberger, T. Sattelmayer, Detonation propagation in hydrogen–air mixtures with transverse concentration gradients, *Shock Waves* 26 (2016) 181–192.
- [50] Q. Li, P. Liu, H. Zhang, Further investigations on the interface instability between fresh injections and burnt products in 2-D rotating detonation, *Comput. Fluids* 170 (2018) 261–272.
- [51] F.A. Bykovskii, S.A. Zhdan, Current status of research of continuous detonation in fuel-air mixtures (review), *Combust. Explos. Shock Waves* 51 (2015) 21–35.
- [52] R. Bluemner, M. Bohon, C.O. Paschereit, E.J. Gutmark, Dynamics of counter-rotating wave modes in an RDC, *Joint Propulsion Conference* (2018), p. 4572.
- [53] R.W. Houim, R.T. Fievisohn, The influence of acoustic impedance on gaseous layered detonations bounded by an inert gas, *Combust. Flame* 179 (2017) 185–198.
- [54] E. Mastorakos, Ignition of turbulent non-premixed flames, *Prog. Energy Combust. Sci.* 35 (2009) 57–97.
- [55] M. Röder, T. Dreier, C. Schulz, Simultaneous measurement of localized heat-release with OH/CH₂O-LIF imaging and spatially integrated OH*chemiluminescence in turbulent swirl flames, *Proc. Combust. Inst.* 34 (2013) 3549–3556.
- [56] Y. Hardalupas, M. Orain, Local measurements of the time-dependent heat release rate and equivalence ratio using chemiluminescent emission from a flame, *Combust. Flame* 139 (2004) 188–207.
- [57] I. Glassman, R.A. Yetter, *Combustion*, Elsevier Science, 2008.
- [58] V.N. Gamezo, T. Ogawa, E.S. Oran, Flame acceleration and DDT in channels with obstacles: effect of obstacle spacing, *Combust. Flame* 155 (2008) 302–315.
- [59] E.S. Oran, V.N. Gamezo, Origins of the deflagration-to-detonation transition in gas-phase combustion, *Combust. Flame* 148 (2007) 4–47.